



Journal of Mining and Environment (JME)

journal homepage: [www.jme.shahroodut.ac.ir](http://www.jme.shahroodut.ac.ir)



## Study of Rock Pillar Failure Consisting of Non-Persistent Joint using Experimental Test and Fracture Analysis Code in Two Dimensions

Vahab Sarfarazi<sup>1\*</sup>, Hosein Karimi javid<sup>1</sup>, and Kaveh Asgari<sup>2</sup>

1. Department of Mining Engineering, Hamedan University of Technology, Hamedan, Iran

2. Department of Mining Engineering, Shahid Bahonar University of Kerman, Kerman, Iran

### Article Info

Received 15 November 2020

Received in Revised form 24 November 2020

Accepted 28 November 2020

Published online 28 November 2020

DOI:10.22044/jme.2020.10266.1968

### Keywords

Fracture analysis code in two dimensions (FRANC2D)

Physical test

Rock pillar

Joint

### Abstract

The experimental and numerical methods were used to investigate the effects of joint number and joint angle on the failure behaviour of rock pillars under a uniaxial compressive test. The gypsum samples with dimensions of 200 mm × 200 mm × 50 mm were prepared. The compressive strength of the intact sample was 7.2 MPa. The imbedded joint was placed inside the specimen. The joint length was 6 cm in a constant joint length. There were several numbers of cracks including one, two, and three cracks. In the experimental tests, the angles of the diagonal plane with respect to the horizontal axis were 0, 30, 60, and 90 degrees. The axial load was applied to the model with a rate of 0.01 mm/s. In the fracture analysis code, the angles of the diagonal plane with respect to the horizontal axis were 0, 15, 30, 45, 60, 75, and 90 degrees. A constant axial load of 135 MPa was applied to the model. The results obtained showed that the failure process was mostly dependent on the angle and number of the non-persistent joint. The compressive strength of the samples was dependent on the fracture pattern and the failure mechanism of the discontinuities. It was shown that the tensile cracks were developed within the model. The strength of the specimens increased by increasing both the joint angle and joint number. The joint angle of 45° KI had the maximum quantity. The stress intensity factor was decreased by increasing the joint number. The failure pattern and failure strength were analogous in both methods, i.e. the experimental testing and the numerical simulation methods.

### 1. Introduction

One way to increase the recovery rate in underground coal mining is to leave no supporting coal pillars in the mining space or reduce their size to the minimum [1]. Designing the coal pillars is a vital factor for a safe and efficient production in coal mines. Figure 1 shows the sliding along two non-persistent joints in a pillar (Esterhuizen, [2]).

Many authors have investigated the coal pillar design, stress analysis, and pillar design method proposed in [3]. In a long-wall logging system, determining the formation of the pillar is essential for the aims of: (1) isolating the exploited panel, and (2) supporting the roadway. Due to different conditions and functions, there are various methods available for the design of coal pillars. Sheorey [3] has proposed three methods for designing and

analyzing pillars: (i) selecting the strength of the pillar from the formula, determining the average load (depending on the one-sided or two-sided goaf, caving or stowing) and the width of pillar with a suitable safety factor; (ii) choosing the width of the pillar so that the roadway is not much affected by the previous mining panel; and (iii) using a numerical model to analyze the stresses with various sizes of coal pillar according to coal seam conditions. The numerical modeling tools have made significant advances in the recent decades, and their ability to simulate the physical phenomena at a wide range of scales as well as the associated computational capabilities has greatly improved. Usually in the field of rock mechanics, large-scale design problems exist; these problems

✉ Corresponding author: [vahab.sarfarazi@gmail.com](mailto:vahab.sarfarazi@gmail.com) (V. Sarfarazi).

are generally geometrically complex and also they are aggravated by the heterogeneous nature of most rock masses. Although the empirical relationships could provide rough design parameters, limitations of the database, used for their development, generally constrained them. In addition, the field-scale experimental programs developed to minimize the need for abstract analyses may be inappropriate due to the associated costs. Among the suitable tools for the purposes of analysis and design, we can mention the numerical modeling tools but the discrete element method (DEM) and the finite-discrete element method (FDEM) are better suited for investigating small-scale rock damage processes (Munjiza, [4]; Jing and Stephansson, [5]; Ghazvinian *et al.* [6]; Lisjak and Grasselli, [7]; Farahmand and Diederichs, [8]; Yan *et al.* [9]; Mayer and Stead, [10]), and continuum approaches remain the primary practical tool for mine-scale simulations. A numerical model for the stress analysis of this problem has been performed in [11-20]. Using the numerical simulations, Lifeng [21] has shown that the distance of the roadway from goaf has some effects on the distribution of stress in the roof of the coal seam, which cannot be calculated using the design formula. Based on the simulated 2D number model, Lifeng [21] has shown that an intermediate value for the pillar width is not suitable for the roadway stability. Mortazavi *et al.* [22] have found from a numerical calculation that pillars behave in different ways during the post-rupture phase regarding the width/height ratio: narrow pillars (low width/height ratio) showed a brittle elastic-plastic behaviour with a remarkable decay of the mean axial stress of the pillar on reaching rupture; squat pillars (a relatively high width/height ratio above the unit) showed an ideal elastic-plastic behaviour with a constant mean axial stress value in the post-rupture phase as the mean axial deformations progressed; very squat pillars (very high width/height ratio, above 1.5) showed hardening the elastic-plastic behaviour with appreciable increases in the mean axial stress as the mean axial deformation progressed in the post-rupture phase. Based on these considerations, the necessity of requesting higher safety factors for narrow pillars that can collapse suddenly once the rupture is reached emerges, while it is possible to assume lower safety factors for squat and very squat pillars, which can however show an elevated strength even in the presence of evident signs of rupture of the pillar. Kaiser and Tang [23] have shown that when the elastic modulus of the rock on the roof of a void is much lower than that of the

rock of the pillars, the rupture phase of a pillar is of a brittle elastic-plastic type as the great energy accumulated by the rock on the roof and on the floor is suddenly discharged onto the pillar until it is ruptured. Jaeger and Cook [24] have sustained that the rupture of the pillar can be violent in these cases, and rock blocks could even be thrown from the side walls. Again, in these cases, given the great risks for the underground workers connected to the rupture of the pillar, it is necessary to foresee high safety factors. Nowadays, the area of influence method cannot be used the dimensions of a rock pillar. Different methods like 3D numerical and analytical modelling [25-35] can be adopted to determine the stress strain state inside the pillar, and therefore, the local safety factors in the rock mass. In the previous research works, the effects of non-persistent joints on the failure behavior of rock pillar have not been studied. In this work, the experimental and numerical methods (fracture analysis code for 2D) were used to investigate the effects of joints number and joint angle on the failure behaviour of rock pillars under a uniaxial compressive test. In the first section, the experimental tests were studied. This section focuses on the sample preparation, testing, and test results. In the second section, the numerical simulation of the failure behavior of rock pillar consisting of non-persistent joint was investigated. In this section, the model preparation, crack generation, and testing results were rendered.



**Figure 1. Sliding along two non-persistent joints in a pillar (Esterhuizen, [2]).**

## 2. Uniaxial compression test for rock-like specimens with non-persistent joints

The rock-like materials were used to simulate the fractured rock masses in these tests. The materials were mixed according to a mass ratio of 2:1 of gypsum:water. The sample dimensions (length \* width \* height) were 20 cm \* 20 cm \* 10 cm. Open cracks were made by pre-inserting a thin metal sheet and removing it after the initial solidification of the specimen (Figure 2). In order to eliminate accidental error and improve the accuracy of the scientific experiment, three identical prefabricated

crack test blocks were prepared for each group. The linear non-persistent cracks were formed in the model. The joint length was 6 cm in a constant joint length. There were several numbers of cracks including one (Figure 3), two (Figure 4), and three (Figure 4) cracks. The angles of diagonal plane with respect to the horizontal axis were 0 (Figure 3a, 4a, and 5a), 30 (Figure 3b, 4b, and 5b), 60 (Figure 3c, 4c, and 5c), and 90 (Figure 3d, 4d, and 5d) degrees. The specimens were placed in a cool and ventilated location for 28 days.

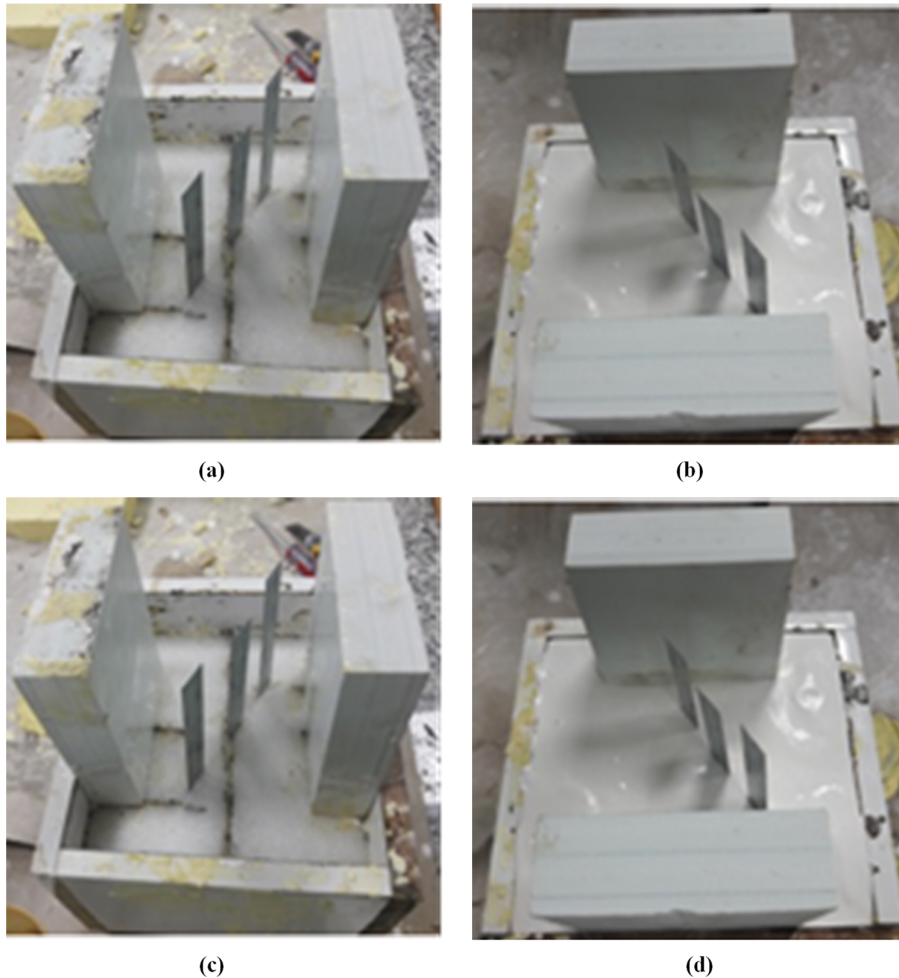


**Figure 2.** a) The frame with dimensions of 200 mm × 200 mm × 100 mm and a special plastic fiber with dimensions of 200 mm × 200 mm × 100 mm were put into the frame, the shim inside the plastic fiber, b) adjustment of the wooden box inside the frame, c) adjustment the shim inside the frame, d) slurry inside the box.

The uniaxial compression test for the non-persistent joints was performed using the electrohydraulic universal test machine. The experimental system consisted of a test bed, the loading control system, and the data acquisition

system. The specimen was placed in the center of the base and kept in a horizontal contact with the base. During the experiment, the displacement loading rate was controlled at 0.01 mm/s (Fig 6).

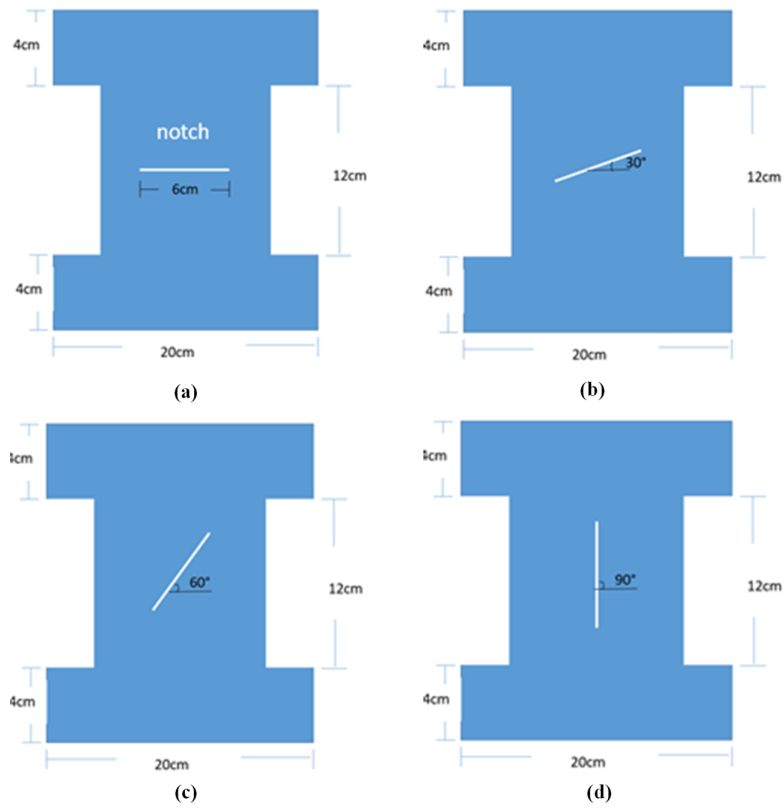


Figure 3. A schematic view of the model consisting of joints with angles of a) 0, b) 30, c) 60, and d) 90 degrees.

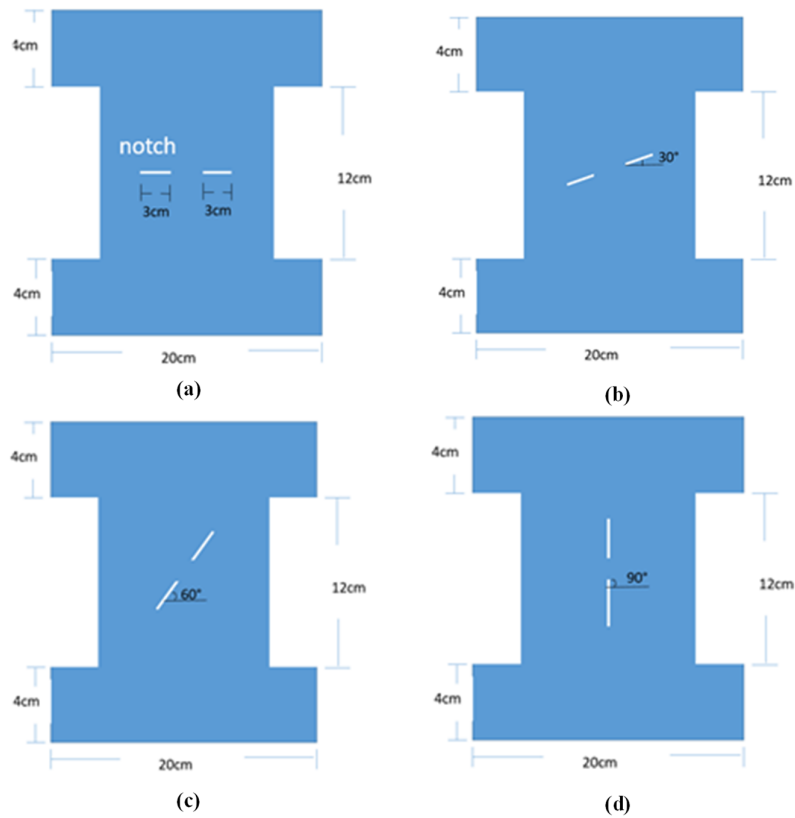


Figure 4. A schematic view of the model consisting of two joints with angles of a) 0, b) 30, c) 60, and d) 90 degrees.

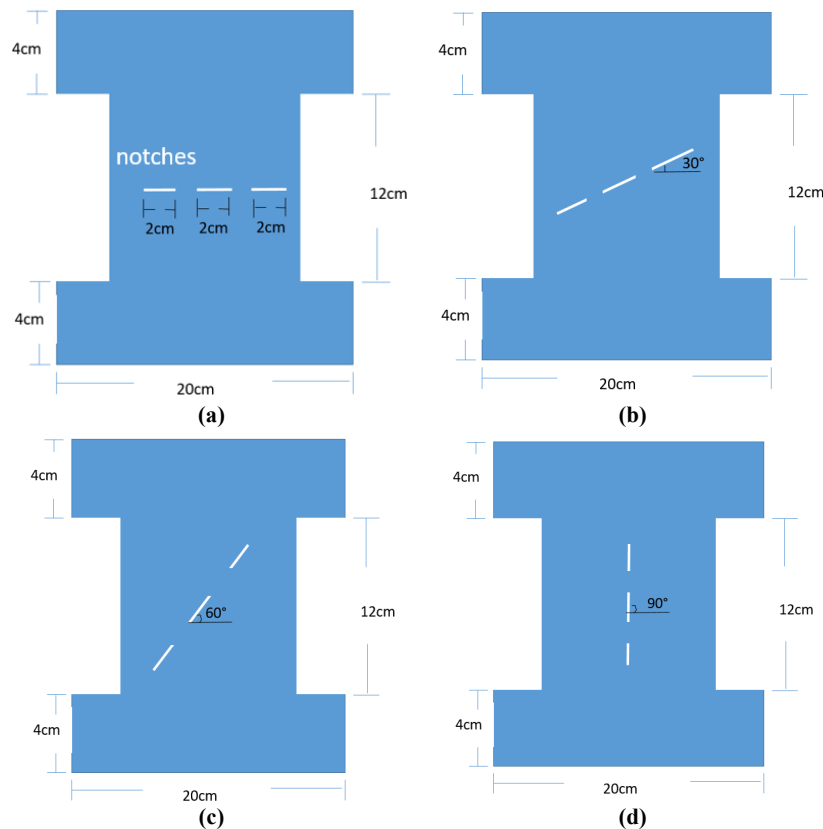


Figure 5. A schematic view of the model consisting of three joint with angle of a) 0, b) 30, c) 60, and d) 90 degrees.

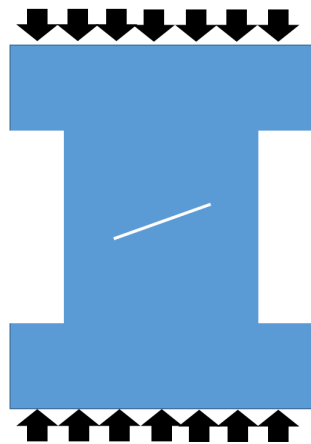


Figure 6. A schematic view of loading the specimen.

### 3. Experimentally observed failure patterns

#### 3.1. Failure pattern of experimental specimens

##### a) Number of imbedded joints was 1

Figure 7 shows the failure pattern of the samples with the oriented plane angles of 0, 30, 60, and 90 degrees. When the joint angle was 0 (Figure 7a),

two tensile wing cracks were originated from the joint walls and scattered parallel to the loading axis till interlocked with the boundaries of the sample. Also two secondary cracks were originated from the joint tips and scattered parallel to the loading axis till interlocked with the the sample walls. When the joint angle was 30 degrees (Figure 7b), two tensile wing cracks were originated from the joint tips and scattered parallel to the loading axis till interlocked with the boundaries of the sample. When the joint angle was 60 degrees (Figure 7c), two tensile wing cracks were originated from the joint tips and scattered parallel to the loading axis till interlocked with the boundaries of the sample. Also two secondary cracks were originated from the joint tips and scattered parallel to the loading axis till interlocked with the the sample walls. When the joint angle was 90 degrees (Figure 7d), the splitting failure occurred in the sample. The joint had no effect on the failure process. In all samples, the failure surface was smooth without the pulverized material. This was representative of the tensile crack.

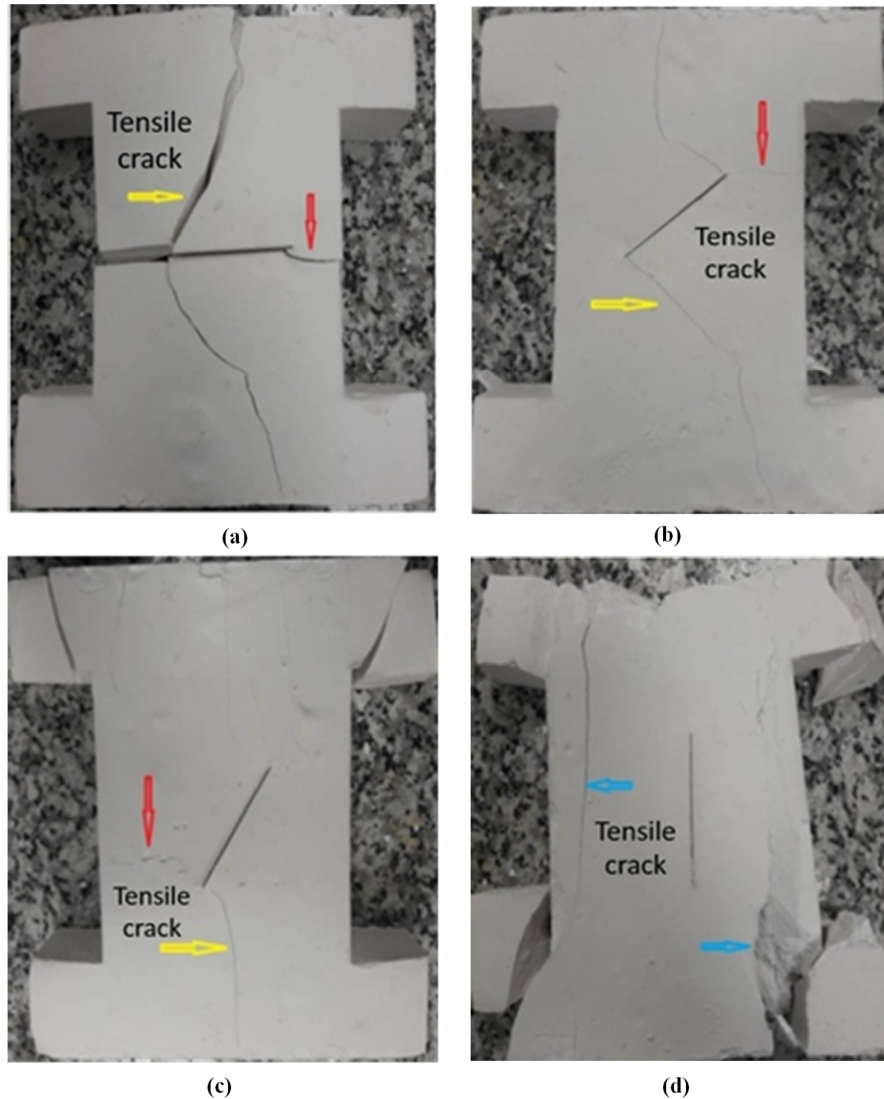


Figure 7. Failure pattern in specimens containing one joint with angles of a) 0, b) 30, c) 60, and d) 90 degrees.

#### b) Number of imbedded joint was 2

Figure 8 shows the failure pattern of the specimens with the oriented plane angles of 0, 30, 60, and 90 degrees. When the joint angle was 0 (Figure 8a), four tensile wing cracks were originated from the joint walls and scattered parallel to the loading axis till interlocked with the boundaries of the specimen. Two other secondary cracks were originated from the outer joint tips and scattered parallel to the loading axis till interlocked with the specimen walls. Also two secondary cracks were originated from the inner joint tips and led to a rock bridge failure. When the joint angles

were 30 and 60 degrees (Figure 8b and 8c), four tensile wing cracks were originated from the outer joint tips and scattered parallel to the loading axis till interlocked with the boundaries of the sample. Also two secondary cracks were originated from the inner joint tips, and led to a rock bridge failure. In these configurations, the gypsum columns were separated from the specimen walls. When the joint angle was 90 gypsum (Figure 8d), a splitting failure occurred in the specimen. The joint had no effect on the failure process. In all samples, the failure surface was smooth without the pulverized material. This was representative of a tensile crack.

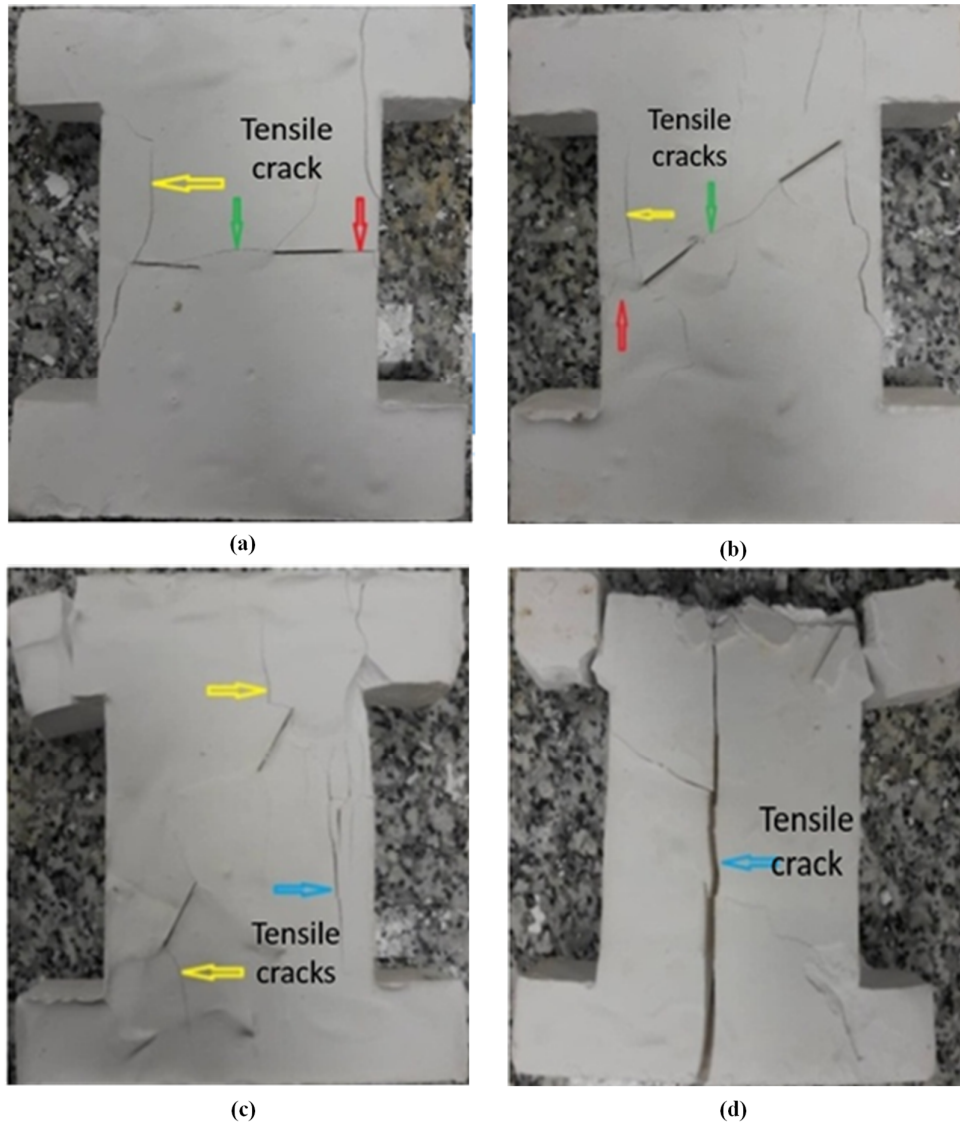


Figure 8. Failure pattern in specimens containing two joints with angles of a) 0, b) 30, c) 60, and d) 90 degrees.

### c) Number of imbedded joint was 3

Figure 9 shows the failure pattern of the specimens with the oriented plane angles of 0, 30, 60, and 90 degrees. When the joint angle was 0 (Figure 9a), four tensile wing cracks were originated from the joint walls and scattered parallel to the loading axis till interlocked with the boundaries of the sample. Two other secondary cracks were originated from the outer joint tips and scattered parallel to the loading axis till interlocked with the sample walls. In addition, four secondary cracks were originated from the inner joint tips, and led to a rock bridge failure. When the joint angles

were 30 and 60 degrees (Figure 9b and 9c), four tensile wing cracks were originated from the outer joint tips and scattered parallel to the loading axis till interlocked with the boundaries of the specimen. Also four secondary cracks were originated from the inner joint tips, and led to a rock bridges failure. In these configurations, the gypsum columns were separated from the sample walls. When the joint angle was 90 degrees (Figure 9d), a splitting failure occurred in the sample. The joint had no effect on the failure process. In all samples, the failure surface was smooth without the pulverized material. This was representative of a tensile crack.

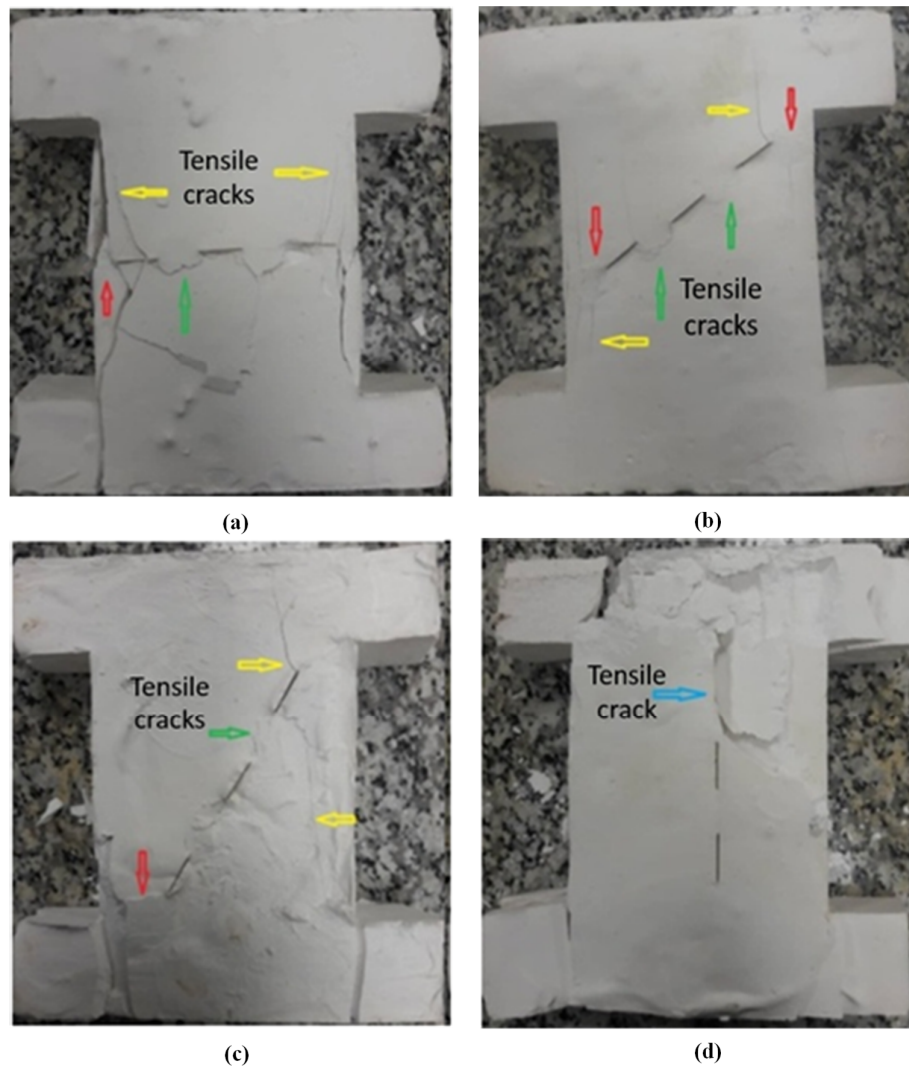


Figure 9. Failure pattern in specimens containing three joints with angles of a) 0, b) 30, c) 60, and d) 90 degrees.

### 3.2. Effects of joint number and joint angle on strength of samples

Figure 10 shows the effect of joint angle on the strength of the models. This figure was presented for three joint numbers. The strength of the specimens was increased by increasing the joint angle. The minimum compressive strength occurred when the joint angle was 30 degrees. The strength of the sample was increased by increasing the joint number. The compressive strength of the intact sample was 7.2 MPa. It shows that the compressive strength of the sample was decreased in the presence of a joint within the sample.

### 4. FRANC software

FRANC is a highly compatible program that can be used to simulate the crack's growth in the layered structures. This program is a FRANC

extension used to enable the display of the layered structures such as the lap joints or bonded repairs. The system used in this software is a standard eight or six noded serendipity elements with functions of quadratic shape. These elements have a good performance in an elastic analysis; furthermore, it is a significant advantage for the stress singularity at the crack tip, which is incorporated in solution by moving the lateral nodes to the quarter-point locations.

The cracks scattering due to the internal or external loadings can be modeled by FRANC. The crack propagation is performed in a predicted direction that has been confirmed by any of the three propagation theories of FRANC. However, the FRANC program is not able to generate the part geometry and networking. Usually piece is modeled by other programs and networking events. Due to this reason, a piece of software components

called CASCA is introduced to perform the network modelling. In the CASCA program, no analysis has been prepared just to calculate the FRANC program. The CASCA program is a program that generates a simple mesh. Although, strictly speaking, it is not part of the FRANC program, it is distributed with FRANC, and can be

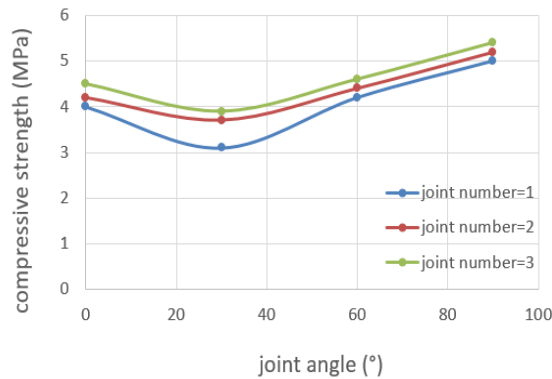


**Figure 10. Effect of joint angle on the strength of models.**

2. The produced mesh in CASCA is then saved as a file, and then the simulation process can be done using FRANC2D.

3. After the file is saved and exited from CASCA, the saved mesh file in CASCA is then opened in FRANC2D.

4. The type of problem and suitable material properties are defined, and the set for the model material command sequence are applied accordingly: PROBLEM TYPE => PLANE STRESS for the material option command MATERIAL is selected. The corresponding quantities of thickness, Young's modulus, and Poisson's ratio are given by selecting the THICKNESS, E, and NU options, respectively.

5. After adjusting the material page, one should reformulate the element stiffness matrices. The ELEM STIFF option is used for this section, and the file is saved.

6. Then the boundary situations are determined by selecting PRE-PROCESS and then FIXITY. The bottom edge is fixed approximately in the X and Y directions. In order to adjust the size of the box containing the node, the tolerance window (below the sheet) is used.

7. After determination of the boundary conditions, the loads are presented by selecting LOADS->DIST LOAD. Then the corresponding

used to generate the initial meshes for the FRANC simulations. The simulation techniques for both aforementioned methods are as follow:

1. The CASCA pre-processor is used to create a geometrical layout of the beam of the required dimensions and a mesh pattern is generated for the same (Figure 11).

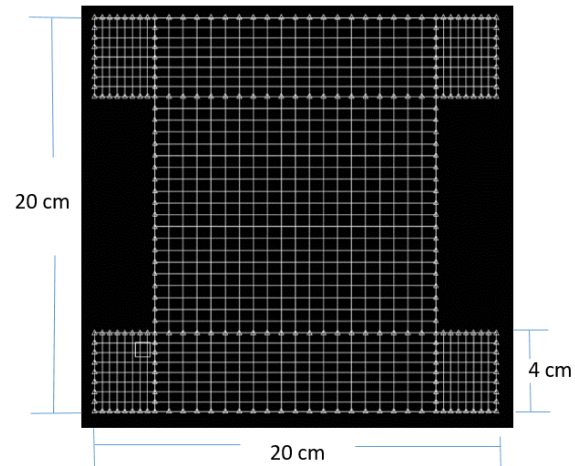


**Figure 11. Mesh generated in Casca2.**

values for load are entered and loading is determined for the simulations.

8. The stress analysis is done by selecting ANALYSIS->LINEAR->DIRECT STIFF. This provides a brief report of the size of the model and the required time for the analysis.

9. For examining the accuracy boundary conditions, after the analysis, the DEFORMD MESH option is used. Then the POST-PROCESS option is selected followed by the CONTOUR option, which provides us with various colour stress contours to indicate the effective stress (EFF STRESS), principle stresses (SIG 1 and SIG 2), shear stress (TAU MAX), etc.

10. Now crack is put in the model. Crack is originated by selecting MODIFY->NEWCRACK->NONCOHESIVE->EDGE CRACK. The crack location is specified in the middle of the model. The crack length is then entered and the minimum number of elements along crack extension is taken as 2. Then ACCEPT option is selected. Re-meshing of the nodes takes place (Fig 12), whereas the opening of notch in the experimental test is 1 mm. Therefore, the joint mechanical properties have no effect on the failure behavior of the rock pillar. In this way, the non-cohesion joint is selected for the numerical simulation.

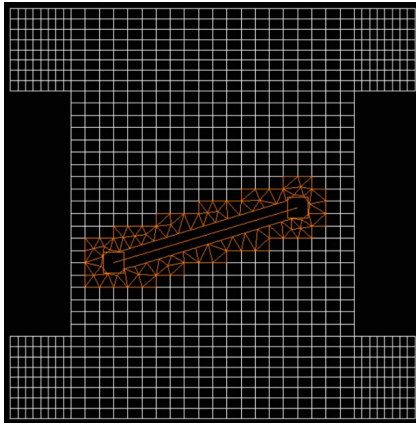


Figure 12. Crack location was specified in the middle of the model.

12. Then the FRACT MECH option is selected, and the J integral technique (J-INTEGRAL), displacement correlation technique (DSP CORR SIF), and modified crack closure technique (MD CRK-CLOS) are used to compute the stress

intensity factors. The results of three techniques gave similar quantities.

13. Now the crack is scattered from the crack tip. This is done by selecting MODIFY > MOVE CRACK > AUTOMATIC. The CRACK INCR option is chosen to give the amount of crack growth at each step, and the crack increment value per step is specified. The number of propagation steps is set using the STEPS option. Then the PROPAGATE option is selected to begin the crack propagation.

14. Then the file is saved using the WRITE option.

15. Now the Stress Intensity Factor option is used to find the stress intensity factor.

#### 4.1. Numerical results:

##### a. principal stress distribution in models ( $\sigma_1$ )

Figure 13 shows the principal stress distribution in the models ( $\sigma_1$ ) with different joint angles. The maximum tensile stress is concentrated at the tip of the joint. The tensile stress had the maximum value when the joint angle is  $45^\circ$ .

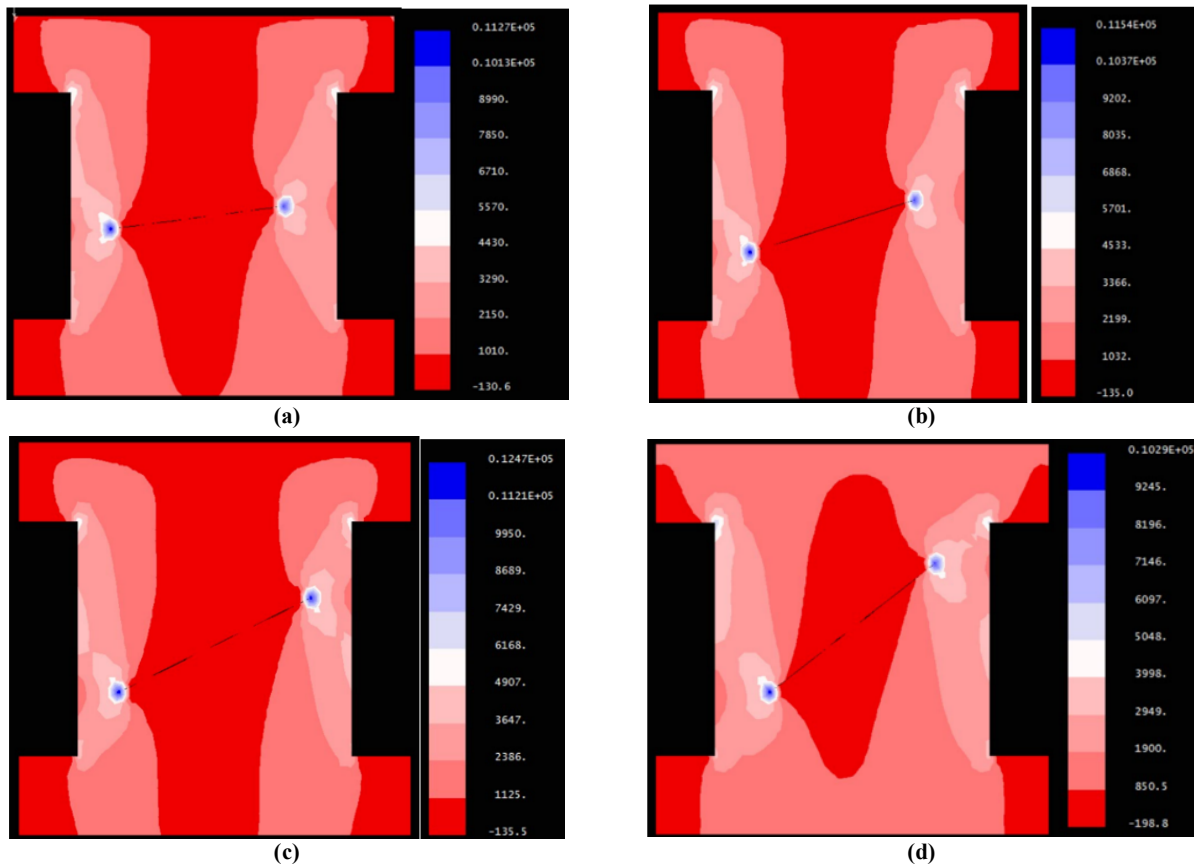
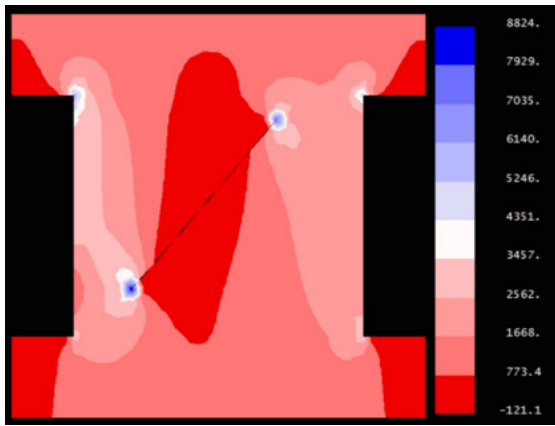
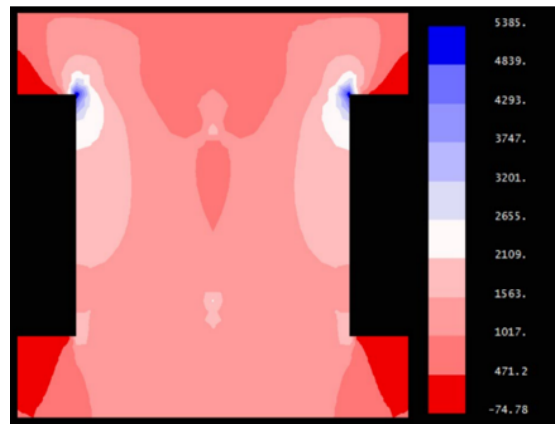


Figure 13. The principal stress distribution in models ( $\sigma_1$ ) with different joint angles of a)  $15^\circ$ , b)  $30^\circ$ , c)  $45^\circ$ , d)  $60^\circ$ .



(e)



(f)

Continuation of Figure 13. e) 75°, and f) 90°.

**b. Effect of joint angle on stress intensity factor (KI)**

Figure 14 shows the effects of joint angle and joint number on the stress intensity factor (KI). KI had the maximum value when the joint angle was 45°. It shows that the crack was originated from this joint in a lower far field stress. The stress intensity factor was decreased with increase in the joint number.

**c. Effects of joint angle and joint number on failure pattern**

Figure 15 shows the effect of the joint angle on the failure pattern. One number of joint was situated in the model. Two wing cracks were

originated from the joint tips and scattered nearly parallel to the loading axis.

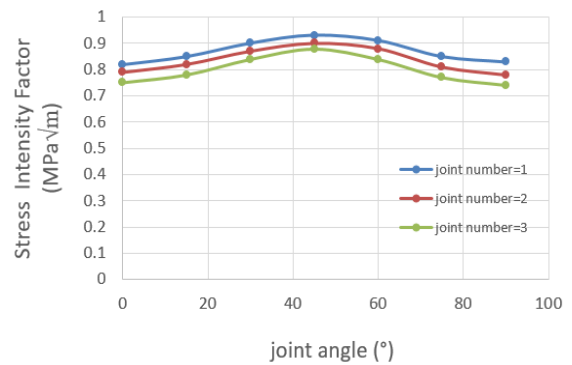
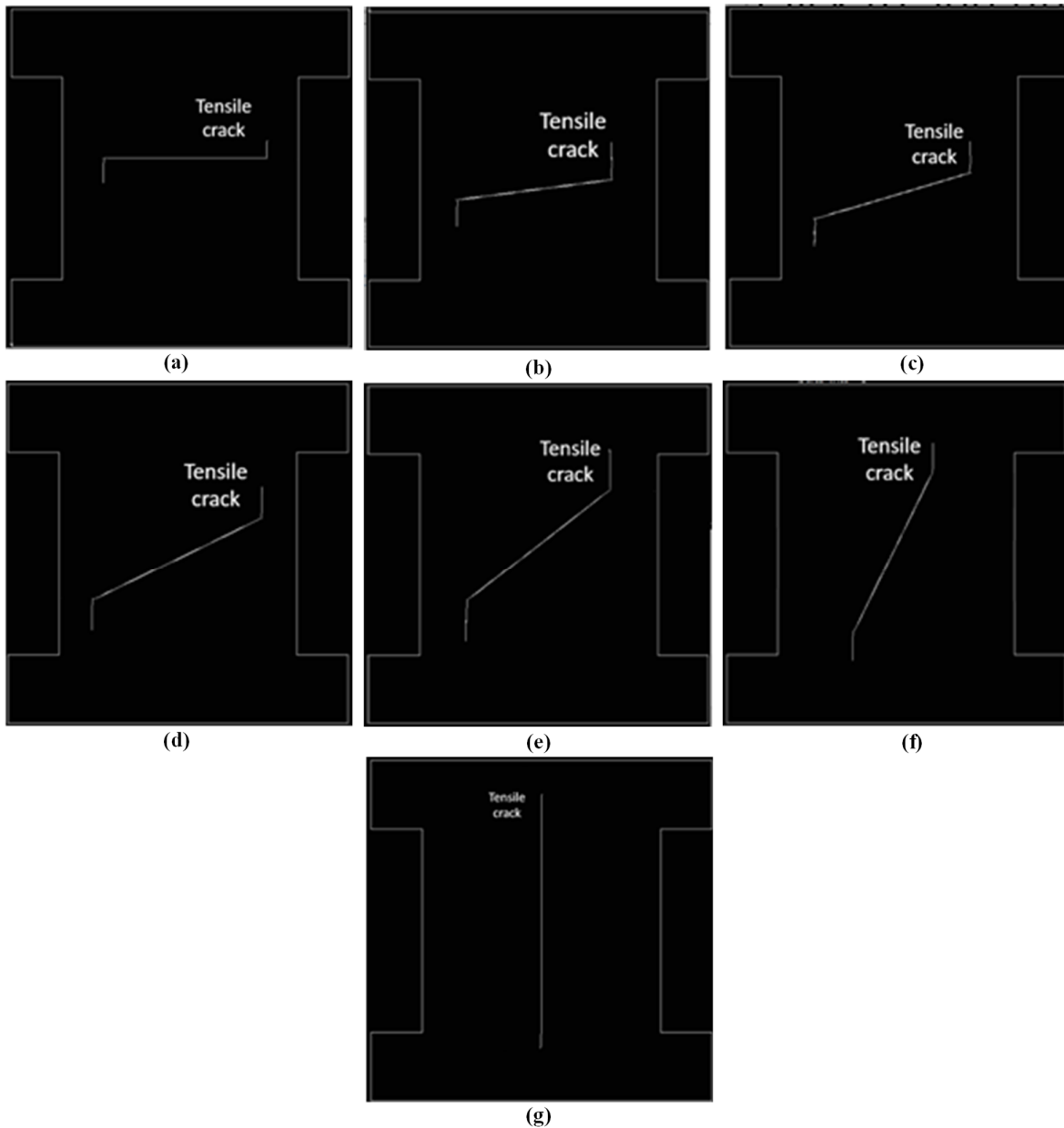


Figure 14. Effect of joint angle on the stress intensity factor (KI).



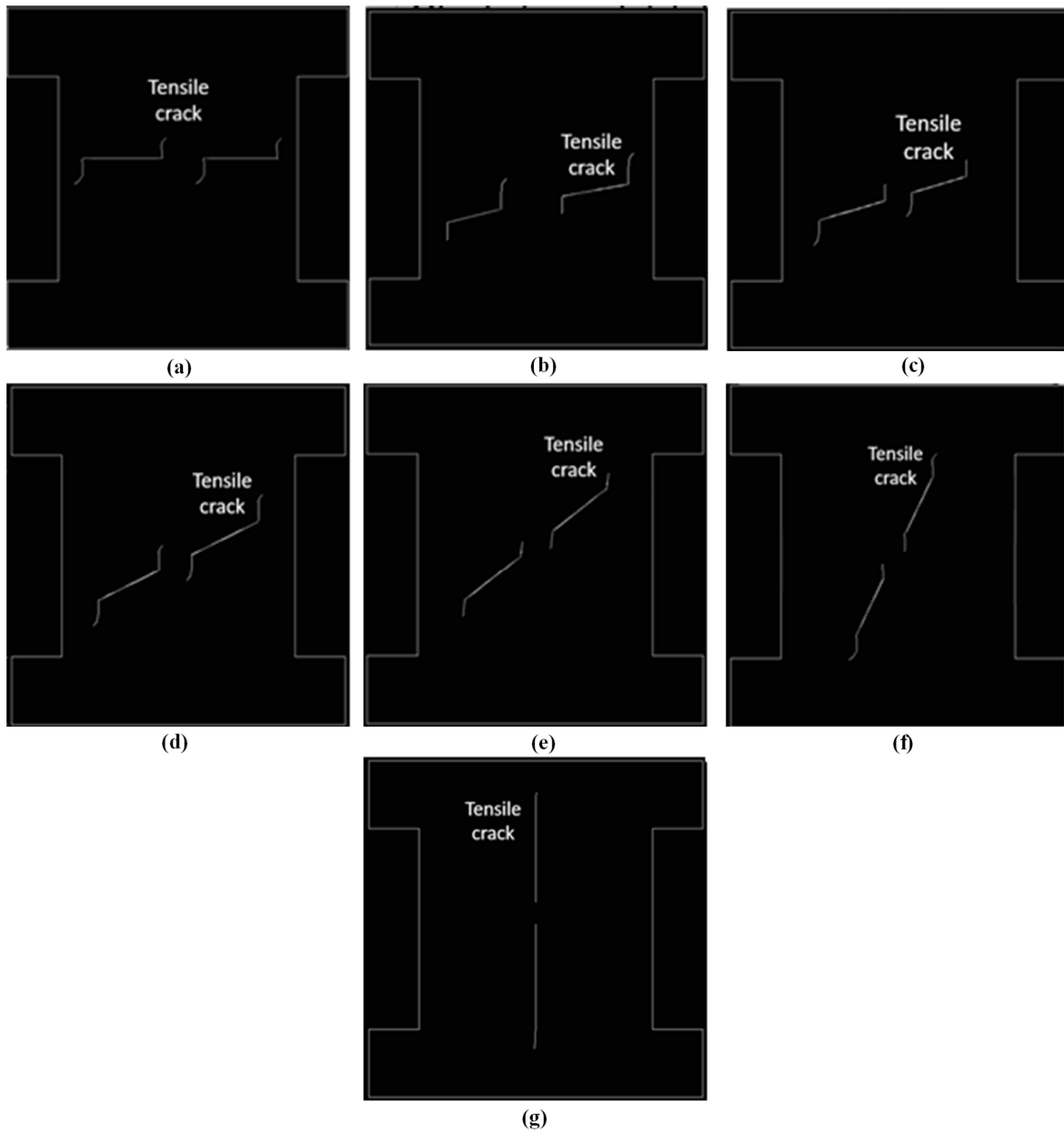
**Figure 15. Failure pattern of models with joint angles of a) 0, b) 15, c) 30, d) 45, e) 60, f) 75, and g) 90 degrees; the number of joints was one.**

Figure 16 shows the effect of joint angle on the failure pattern. Two numbers of joints were situated in the model. Four wing cracks were originated from the joint tips and scattered nearly parallel to the loading axis.

Figure 17 shows the effect of joint angle on the failure pattern. Three numbers of joints were

situated in the model. Six wing cracks were originated from the joint tips and scattered nearly parallel to the loading axis.

By comparison between Figure 7-9 and Figure 15-17, it could be concluded that the same failure mode occurred in the experimental tests and numerical simulation.



**Figure 16.** Failure pattern of models with joint angles of a) 0, b) 15, c) 30, d) 45, e),60, f) 75, and g) 90 degrees; the number of joints was two.

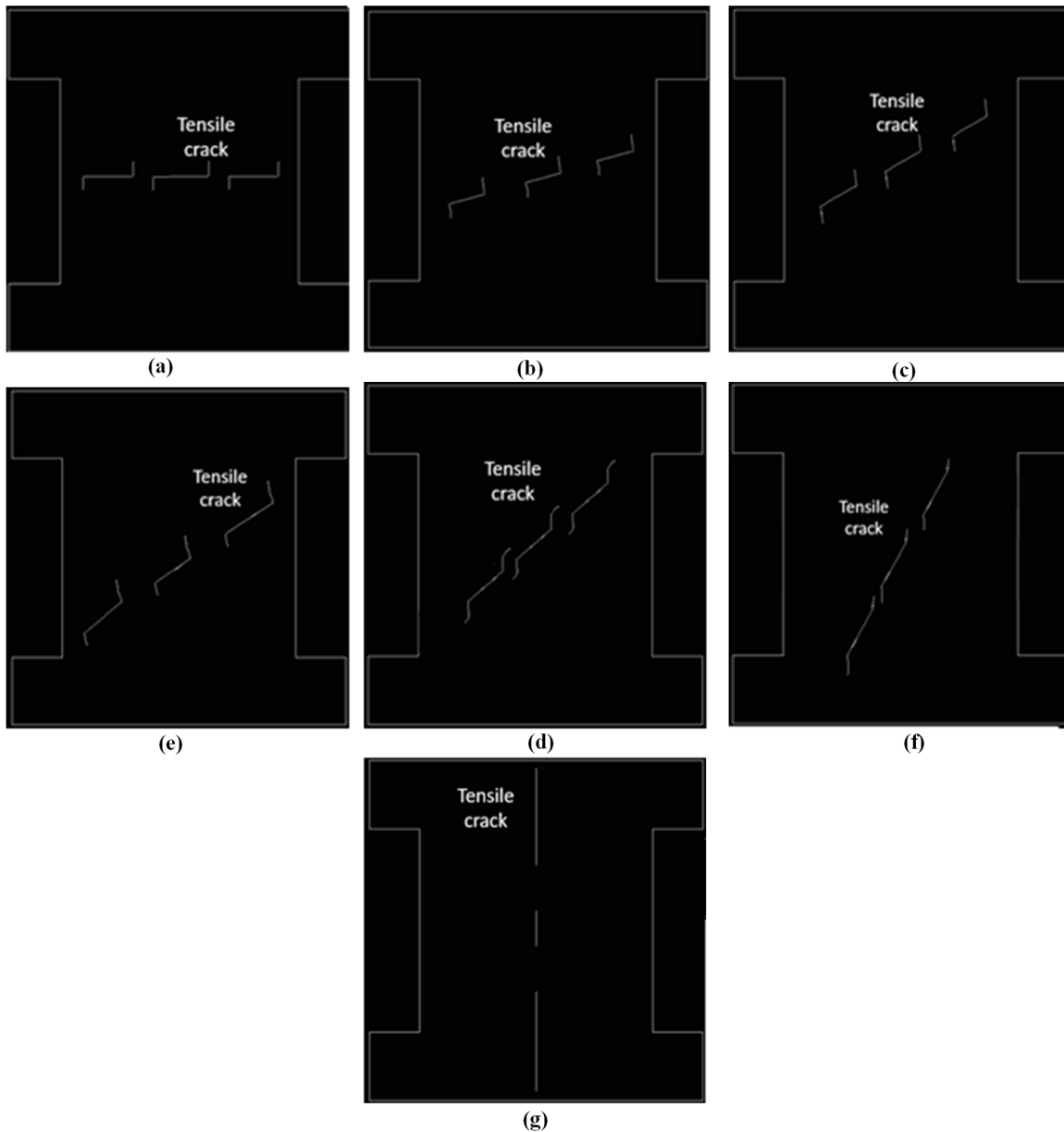


Figure 17. Failure pattern of models with joint angles of a) 0, b) 15, c) 30, d) 45, e) 60, f) 75, and g) 90 degrees; the number of joint was three.

## 5. Conclusions

The experimental and discrete element methods were used to investigate the effects of joints number and joint angle on the failure behaviour of rock pillars under a uniaxial compressive test. The gypsum samples with dimensions of  $200 \text{ mm} \times 200 \text{ mm} \times 50 \text{ mm}$  were prepared. The compressive strength of the model material was 7.2 MPa. The imbedded joints were placed inside the specimen. The joint length was 6 cm. In a constant joint length, there were several numbers of cracks including one, two, and three cracks. In the experimental test, the angles of diagonal plane with

respect to the horizontal axis were 0, 30, 60, and 90 degrees. In the numerical test, the angles of the diagonal plane with respect to the horizontal axis were 0, 15, 30, 45, 60, 75, and 90 degrees. The axial load was applied to the model by a rate of 0.05 mm/min. The results obtained showed that the followings:

- **When the joint angle was less than 75**

When the joint angle was 15, two tensile wing cracks were originated from the outer joint tips and distributed diagonal to the loading axis till integrated with the boundaries of the sample. Also two wing cracks were originated from the inner

joint tips and scattered diagonally till integrated with the hole wall. Two vertical tensile cracks were originated from the joint walls and scattered parallel to the loading axis till integrated with the sample boundary. When the joint angle was 30 degrees, one tensile wing crack was originated from the outer tip of the left joint and distributed diagonal to the loading axis till integrated with the boundaries of the sample. Also two vertical tensile cracks were originated from the joint walls and scattered parallel to the loading axis till integrated with sample boundary. When the joint angle was 45 degrees, one tensile wing crack was originated from the outer tip of the right joint and distributed diagonal to the loading axis till integrated with the boundaries of the sample. Also two vertical tensile cracks were originated from the joint walls and scattered parallel to the loading axis till integrated with the sample boundary. In these conditions, the rock bridges were broken during the test. The failure surface was smooth without the pulverized material. This was representative of the tensile crack.

- **When the joint angle was more than 75**

In the crack initiation stage, two tensile cracks were originated from the joint tip and scattered parallel to the loading axis. In the final stage, several shear bands were developed in the model and led to a failure of the model. In this condition, the presence of joint had no effect on the fracture propagation.

- The area of the “v” shape column was increased by increasing the joint angle from 0 to 60 degree
- The area of the failure surface of rock bridge decreased by increasing the joint angle.
- The wing crack angle with respect to the joint plane decreased by increasing the joint angle.
- The strength of the samples was increased by increasing the joint angle.
- The minimum compressive strength occurred when the joint angle was 30 degrees.
- In a constant joint length, the strength of the sample was increased by increasing the joint number.
- The maximum tensile stress was concentrated at the tip of the joint. The tensile stress had the maximum value when the joint angle was 45°.
- KI had the maximum value when the joint angle was 45°. It showed that the crack was originated from this joint in a lower far field stress. The

stress intensity factor was decreased by increasing the joint number.

- The failure mode was similar in both the experimental test and the numerical simulation.

## References

- [1]. Bieniawski Z. T., Van Heerden W. L., (1975) The significance of *in situ* tests on large rock specimens Int J Rock Mech Min Sci Geomech, 12, 101.
- [2]. Esterhuizen GS. (2006) Evaluation of the strength of slender pillars. Trans Soc Min Explor Geol 2006; 320:69–76.
- [3]. P. R. Sheorey, (1993) Design of coal pillar arrays and chain pillars, Comprehensive rock engineering, 2, 631.
- [4]. Munjiza A. The combined finite-discrete element method. John Wiley and Sons Inc. ; 2004.
- [5]. Jing L, Stephansson O. Fundamental of discrete element methods for rock engineering: theory and application. Amsterdam, Netherland: Elsevier; 2007.
- [6]. Ghazvinian E, Diederichs MS, Quey R. 3D random Voronoi grain-based models for simulation for brittle rock damage and fabric-guided micro-fracturing. Journal of Rock Mechanics and Geotechnical Engineering 2014; 6(6):506e21.
- [7]. Lisjak A, Grasselli G. A review of discrete modeling techniques for fracturing processes in discontinuous rock masses. Journal of Rock Mechanics and Geotechnical Engineering 2014; 6(4):301e14.
- [8]. Farahmand K, Diederichs MS. A calibrated synthetic rock mass (SRM) model for simulating crack growth in granitic rock considering grain scale heterogeneity of polycrystalline rock. In: Proceedings of the 49th U.S. rock mechanics/geomechanics symposium. San Francisco, California: American Rock Mechanics Association; 2015. ARMA-2015-430.
- [9]. Yan C, Zheng H, Sun G, Ge X. (2016) Combined finite-discrete element method for simulation of hydraulic fracturing. Rock Mechanics and Rock Engineering 2016; 49(4):1389e410.
- [10]. Mayer JM, Stead D. Exploration into the causes of uncertainty in UDEC grain boundary models. Computers and Geotechnics 2017; 82:110e23.
- [11]. Fadeev A. B., E. K. Abdylidayev, Rock Mech., (1979) Elastoplastic analysis of stresses in coal pillars by finite element method 11, 243.
- [12]. R, J ,Pine, R. Trueman, (1993) Numerical modelling as an aid to the determination of the stress distribution in the goaf due to longwall coal mining Int. J. Rock Mech. Min. Sci. Geomech., 30, 1403.
- [13]. C. Mukherjee, P. R. Sheorey, K. G. Sharma, (1994) Numerical simulation of caved goaf behaviour in

longwall workings. *Int. J. Rock Mech. Min. Sci. Geomech.*, 31, 35.

[14]. G. Murali Mohan, P. R. Sheorey, A. Kushwaha, (2001) Numerical estimation of pillar strength in coal mines *Int. J. Rock Mech. Min. Sci.*, 38, 1185.

[15]. A. Jaiswal, S. K. Sharma, B. K. Shrivastva, (2004) Numerical modeling study of asymmetry in the induced stresses over coal mine pillars with advancement of the goaf line *Int. J. Rock Mech Min. Sci.*, 41, 859 (2004).

[16]. Li W., Bai J., Peng S. *et al.*, (2015) "Numerical modeling for yield pillar design: a case study". *Rock Mechanics & Rock Engineering*, 48(1), pp. 305-318.

[17]. Zhang G. C., He F L, Jia H G *et al.*, (2017) "Analysis of gateroad stability in relation to yield pillar size: a case study". *Rock Mechanics & Rock Engineering*, 50(5), 2017, pp. 1-16.

[18]. Shabanimashcool M., Li C. C., (2012) Numerical modelling of longwall mining and stability analysis of the gates in a coal mine. *International Journal of Rock Mechanics & Mining Sciences*, 51(4), 2012, pp. 24-34.

[19]. Peng L. J., Zhang D. F., Guo Z. B. *et al.*, (2013) Numerical analysis of thick coal seam small pillar along gob roadway and its application". *Rock and Soil Mechanics*, 34(2), pp. 36093617.

[20]. Yu B., Zhang Z., Kuang T. *et al.*, (2016) "Stress changes and deformation monitoring of longwall coal pillars located in weak ground". *Rock Mechanics & Rock Engineering*, 49(8), 2016, pp. 32933305.

[21]. L. Lifeng, G. Weili, J. Wang, H.n Deng, Q. Jiang and Y. Liu, (2018) Coal Pillar Width Design in High-stress Gob-side Entry Driving *Journal of Engineering Science and Technology*, 11, 52.

[22]. Mortazavi, A., Hassani, F.P., and Shabani, M. \A numerical investigation of rock pillar failure mechanism in underground openings", *Computers and Geotechnics*, 36(5), pp. 691-697 (2009).

[23]. Kaiser, P.K. and Tang, C.A. \Numerical simulation of damage accumulation and seismic energy release during brittle rock failure", Part II: Rib Pillar Collapse. *International Journal of Rock Mechanics & Mining Sciences*, 35(2), pp. 123-134 (1998).

[24]. Jaeger, J.C. and Cook, N.G.W., *Fundamentals of Rock Mechanics*, 4th Edn., p. 513, Blackwell Publishing, London (2007).

[25]. Do, N.A., Dias, D., Oreste, P., and Djeran-Maigre I. \2D numerical investigation of segmental tunnel lining behaviour", *Tunnelling and Underground Space Technology*, 37, pp. 115-127 (2013).

[26]. Do, N.A., Dias, D., Oreste, P., and Djeran-Maigre, I. \Three-dimensional numerical simulation for mechanized tunnelling in soft ground: The influence of the joint pattern", *Acta Geotechnica*, 9(4), pp. 673-694 (2014).

[27]. Do, N.A., Dias, D., Oreste, P., and Djeran-Maigre, I. \Three-dimensional numerical simulation of a mechanized twin tunnels in soft ground", *Tunnelling and Underground Space Technology*, 42, pp. 40-51 (2014).

[28]. Ranjbarnia, M., Oreste, P., and Fahimifar, A. \Analytical-numerical solution for stress distribution around tunnel reinforced by radial fully grouted rockbolts", *Int. J. Numer. Anal. Meth. Geomech*, 40(10), pp. 1844-1862 (2016).

[29]. Yaylacı Murat, Avcar Mehmet (2020). Finite element modeling of contact between an elastic layer and two elastic quarter planes. *Computers and Concrete*, Vol. 26, No. 2 (2020) 107-114, DOI: <https://doi.org/10.12989/cac.2020.26.2.000>.

[30]. Uzun Yaylacı, E., Yaylacı, M., Ölmez, H. and Birinci, A., (2020). Artificial Neural Network Calculations for A Receding Contact Problem, *Computers and Concrete*, Vol. 25, 6, <https://doi.org/10.12989/cac.2020.25.6.000>.

[31]. Yaylacı Murat, Terzi Cemalettin, Avcar Mehmet (2019). Numerical analysis of the receding contact problem of two bonded layers resting on an elastic half plane. *Structural Engineering and Mechanics*, 72 (6), Doi: 10.12989/sem.2019.72.6.000.

[32]. Öner Erdal, Yaylacı Murat, Birinci Ahmet (2015). Analytical solution of a contact problem and comparison with the results from FEM. *Structural Engineering And Mechanics*, 54(4), 607-622., Doi: 10.12989/sem.2015.54.4.000.

[33]. Yaylacı Murat, Birinci Ahmet (2013). The receding contact problem of two elastic layers supported by two elastic quarter planes. *Structural Engineering and Mechanics*, 48(2), 241-255., Doi: 10.12989/sem.2013.48.2.241.

[34]. Yaylacı Murat, Öner Erdal, Birinci Ahmet (2014). Comparison between Analytical and ANSYS Calculations for a Receding Contact Problem. *Journal of Engineering Mechanics-ASCE*, 140(9), 4014070, Doi: 10.1061/(ASCE)EM.1943-7889.0000781.

[35]. Adiyaman Gökhan, Birinci Ahmet, Öner Erdal, Yaylacı Murat (2016). A receding contact problem between a functionally graded layer and two homogeneous quarter planes. *Acta Mechanica*, 227(3), Doi: 10.1007/s00707-016-1580-y.

## مطالعه شکست پایه سنگی حاوی درزه‌های ناممتد با استفاده از آزمون آزمایشگاهی و کد آنالیز شکست دو بعدی

وهاب سرفرازی<sup>۱\*</sup>، حسین کریمی جاوید<sup>۱</sup> و کاوه عسگری<sup>۲</sup>

۱- گروه مهندسی معدن، دانشگاه صنعتی همدان، همدان، ایران  
 ۲- بخش مهندسی معدن، دانشگاه شهید باهنر کرمان، کرمان، ایران

ارسال ۲۰۲۰/۱۱/۱۵، پذیرش ۲۰۲۰/۱۱/۲۸

\* نویسنده مسئول مکاتبات: sarfarazi@hut.ac.ir

### چکیده:

در این مقاله تاثیر تعداد و زاویه درزه‌های ناممتد بر رفتار شکست پایه‌های سنگی تحت تنش تک محوره بررسی شده است. نمونه‌های گچ با ابعاد  $50 \times 200 \times 200$  mm آماده شد. مقاومت فشاری نمونه‌های بکر  $7/2$  MPa است. درزه محصور با طول  $6$  cm در نمونه ایجاد شد. در طول ثابت درزه، تعداد درزه‌ها متغیر می‌باشد، ۱، ۲ و ۳ عدد. در آزمون‌های آزمایشگاهی، زاویه بین درزه و افق، صفر،  $30^\circ$  و  $90^\circ$  درجه است. نرخ بار محوری اعمال شده به نمونه  $0/01$  mm/s است. در مدلسازی عددی، زاویه بین درزه و افق صفر،  $15^\circ$ ،  $30^\circ$ ،  $45^\circ$ ،  $60^\circ$  و  $90^\circ$  درجه است. تنش  $135$  MPa به مدل عددی اعمال شد. نتایج نشان می‌دهند که پروسه شکست تابع زاویه داری و تعداد درزه‌های ناممتد است. مقاومت فشاری نمونه‌ها به الگوی شکست و مکانیزم شکست درزه‌ها بستگی دارد. ترک‌های کششی، مود غالب شکست هستند که در نمونه اتفاق می‌افتد. با افزایش زاویه داری و تعداد درزه‌ها، مقاومت فشاری نمونه‌ها افزایش می‌یابد. در زاویه درزه  $45^\circ$  درجه، فاکتور شدت تنش کششی ماکزیمم است. فاکتور شدت تنش با افزایش درزه‌ها کاهش می‌یابد. الگوی شکست و تنش شکست نمونه‌ها در مدلسازی عددی و آزمون‌های آزمایشگاهی یکسان است.

**کلمات کلیدی:** کد آنالیز شکست دو بعدی، آزمون فیزیکی، پایه سنگی، درزه.